

# Modelling and Minimization of the Parasitic Capacitances of Single-Layer Toroidal Inductors

Florentin Salomez, Arnaud Videt, and Nadir Idir

**Abstract**—High-frequency power converters need electromagnetic interferences filters using common and differential mode chokes with low parasitic capacitance to comply with the electromagnetic compatibility standards. This paper proposes a modelling method of this capacitance and ways to minimize it. The studied components are ring core inductors with magnetic materials considered as perfect conductors or with high permittivity, such as nano-crystalline material and most Mn-Zn ferrite materials. In comparison to other work in the literature, the proposed approach takes into account the curvature of the turn in addition to the coating of the core and the insulation layer of the wire. The hypotheses, used in this work to simplify the real geometry, are compatible with two dimensional approaches to compute the parasitic inter-turns and turn-core capacitances. These capacitances are evaluated thanks to the 2D finite element method. The obtained model allows accurate evaluation of the effect of turn-core space on the parasitic capacitance, and enables to reduce its value with a limited impact on the volume of the magnetic component.

**Index Terms**—Modelling, Equivalent Parallel Capacitance (EPC), inductor, Electromagnetic Compatibility (EMC), Common-Mode Chokes, Parasitic Capacitance

## I. INTRODUCTION

WIDE-BANDGAP power transistors, made with SiC and GaN, allow the development of high-frequency (up to MHz ranges) static converters. However, these converters produce high-frequency noises, both conducted and radiated, that must be mitigated to respect the Electromagnetic Compatibility (EMC) standards [1], [2]. Among many other techniques [3], a passive filter is often used to change the propagation path of the conducted emissions, thus reducing the impact of the noise, produced by the converter, toward the grid [2], [4]. Since the bandwidth of the conducted EMC standards spans along several decades (hundreds of kHz to hundreds of MHz), a good knowledge of the parasitics of the Electromagnetic Interference (EMI) filter is required to size it correctly [5]–[8]. In this paper, the model of the equivalent parallel capacitance (EPC) of a ring core inductor is considered, along with means of reducing and tuning its value.

In the literature, several models based on Finite Element Method (FEM) and on the modelling of the full geometry have been used to determine the value of the EPC for rod core [9], ring core [10], [11] and spiral inductors [12], [13]. But the difficulty with this numerical approach lays in the deduction of the relation between geometrical and material properties, and the overall value of the EPC. To tackle this

drawback, and to decrease the computation cost of simulations for optimization purpose [4], several analytical models have been developed. Most works reviewed hereafter compute the EPC in two steps:

- 1) the evaluation of the elementary parasitic capacitive coupling between turns, between layer of turns, between turns and core in the middle and at the periphery of the winding;
- 2) the resolution of the capacitance network.

For the first step, layers of winding can be assumed as equivalent cylinder capacitances as in [14]–[16]. These works are dedicated to multilayer winding transformers with straight core, but this approach has been used in [17] to study fractional winding scheme on ring core. Nevertheless it is generally not accurate enough for loose winding made with round conductors. In the literature this problem is solved with image theory [18], equivalent segment or arc parasitic capacitances [19]–[22], a combination of the two previous methods [23], conformal transform [24], or 2D FEM [25], [26]. The latter approach will be used in this paper because it takes into account insulation layers, coating, inter-turn and turn-core spaces.

Then for the second step, the popular model developed by *Massarini et al.* [19] and the derived ones [22], [27] consider a pure capacitive network decoupled from the magnetic part of the component to compute the EPC. But as shown in [25] the evolution of the EPC with the number of turns is not correctly reproduced. A more accurate hypothesis based on energy conservation and presented in several published works [14]–[16], [18], [25], [26], [28], [29], will be used here.

In addition to the modelling of the EPC, some articles propose ways to reduce it. The authors of [23] have identified the turn-core capacitance as the most important one in the total EPC, and its dependence with the inter-turns space. Therefore they suggest to keep the winding tight to avoid the increase of the parasitic capacitive coupling between turns and core, and thus to reduce the EPC, (this has been confirmed in [18], [25], [26]). According to them, for this same reason the turn-core capacitance on the periphery of the winding can not be neglected in the total EPC. Another way to reduce the EPC is to increase the space between turns and core, or between layers thanks to a plastic bobbin as proposed by [15], [30], or by wave-winding technique as done by radio-frequency engineers in the sixties [31]. A last innovative solution has been presented in [8], where the winding is shielded with aluminium foil to the ground to increase the coupling with it, and reduce the coupling across the component. This solution is dedicated to common mode chokes.

The authors are with the Univ. Lille, Arts et Metiers Institute of Technology, Centrale Lille, Junia, ULR 2697 - L2EP, F-59000 Lille, France (e-mail: florentin.salomez@univ-lille.fr; arnaud.videt@univ-lille.fr; nadir.idir@univ-lille.fr).

Manuscript received Month DD, 202x; revised Month DD, 202x.

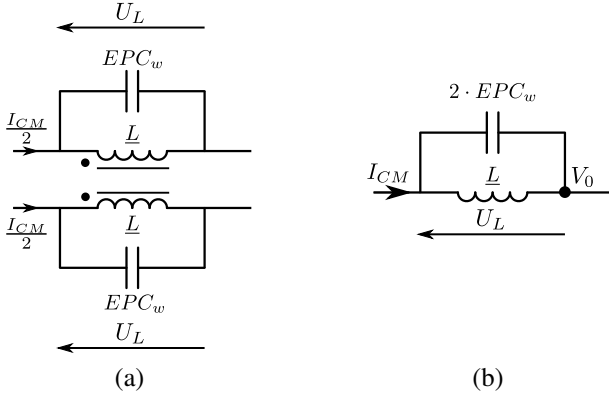


Fig. 1. Equivalent circuits of a common mode inductor with EPC: (a) two phases equivalent circuit, (b) single-phase common mode equivalent circuit.

In this paper a modelling method of the parasitic capacitances to determine the EPC of inductors is proposed. In comparison to the previously reviewed works, the proposed method will focus on the assumptions required to approximate the curvature of both the turns and the coating thickness. In addition it will take into account turn-core and inter-turn spaces to evaluate the possibility to reduce the value of the EPC while keeping the impact on the volume low. The simplified 2D geometry is then used as input of the 2D FEM simulations of the parasitics capacitances. Furthermore, a novel method is proposed to evaluate the applicability of the model for a given magnetic material, notably for ferrite ones where core permittivity is a key parameter.

This paper is structured as follow: Section II presents the models of the EPC and of the parasitic capacitances, with a focus on the compensation of the turn and coating curvatures in this article. Section III shows the experimental validations of the proposed model on conducting magnetic materials like nanocrystalline. Section IV explores applicability of the model to Mn-Zn ferrite materials. Finally Section V deals with the reduction of the EPC by tightening the winding, and by the use of specific plastic spacers. The extension of the model to take into account bigger turn-core spaces than conventional component without spacers will be also presented in this last section.

## II. MODEL OF THE EPC

First, in this section, the electrical couplings occurring in the winding and with the core are explained and an equivalent parallel capacitance is determined as the one added to the circuit representation of a common mode chokes presented in Fig. 1(a) and called  $EPC_w$ , with  $\underline{L}$  the inductance with its losses,  $I_{CM}$  the common-mode current and  $U_L$  the voltage across the component. Second, the geometry of the component and the hypotheses used to transform it to a 2D equivalent one are described in details. Lastly the 2D FEM simulation setups used to retrieve the values of the elementary parasitic capacitances are presented.

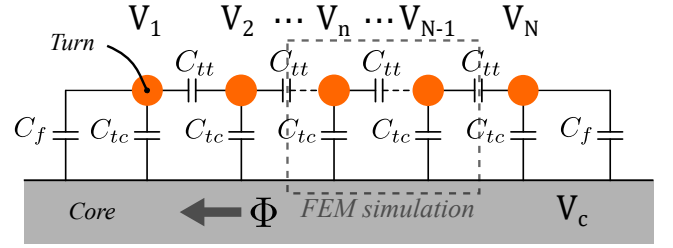


Fig. 2. Equivalent capacitive network of the winding.

### A. Capacitive network of the winding

Parasitic capacitance appears between two conductive surfaces at different potentials. For the inductor, those are the core and the wire. Each turn of the winding is considered as a mono-potential closed loop, hence a turn-core capacitance  $C_{tc}$  and a turn-turn capacitance  $C_{tt}$  are associated with each turn, as depicted in Fig. 2. At the beginning and at the end of the winding there is an additional coupling with the core due to the remaining space without winding, where electric field can further spread, modelled here by a fringe capacitance  $C_f$ .

The equivalent potential  $V_n$  of each  $n$  turn is defined as the mean potential across it, as presented in (1), with  $U_L$  the total voltage across the component, and  $V_0$  a reference potential. Each loop sees the same voltage drop because of the Lenz law, as discussed in [18], [25], [26], [32] and under the hypothesis that no propagation along the wire occurs at the considered frequencies. The core is floating and according to circuit theory the symmetry of the capacitive network leads to a core potential  $V_c$  equal to the mean potential across the component, as defined in (2).

Knowing the voltage across each capacitance, one can find the total electrical energy stored in the winding. Then by equalizing it to the energy held by an Equivalent Parallel Capacitance across the component as in [14]–[16], [18], [25], [26], [28], [29], [32], one can deduce the expression of the winding capacitance  $EPC_w$  as a function of the total number of turns  $N$ , and elementary capacitances  $C_{tc}$ ,  $C_{tt}$  and  $C_f$ , as described in (3). As depicted in Fig. 1(b) for a two winding components excited in common-mode, the overall  $EPC$  is simply two times the  $EPC_w$ .

$$1 \leq n \leq N, \quad V_n = \frac{2n-1}{2N} U_L + V_0 \quad (1)$$

$$V_c = \frac{U_L}{2} + V_0 \quad (2)$$

$$EPC_w(N) = \frac{N-1}{N^2} C_{tt} + \frac{1}{12} \frac{N^2-1}{N} C_{tc} + \frac{1}{2} \left( \frac{N-1}{N} \right)^2 C_f \quad (3)$$

In this article, the case of a coated ring core is studied. To retrieve the values of the elementary parasitic capacitances, the 2D FEM simulations will be performed on a pair of turns as shown in Fig. 2. But first the turn and coating curvatures are compensated in the next subsection.

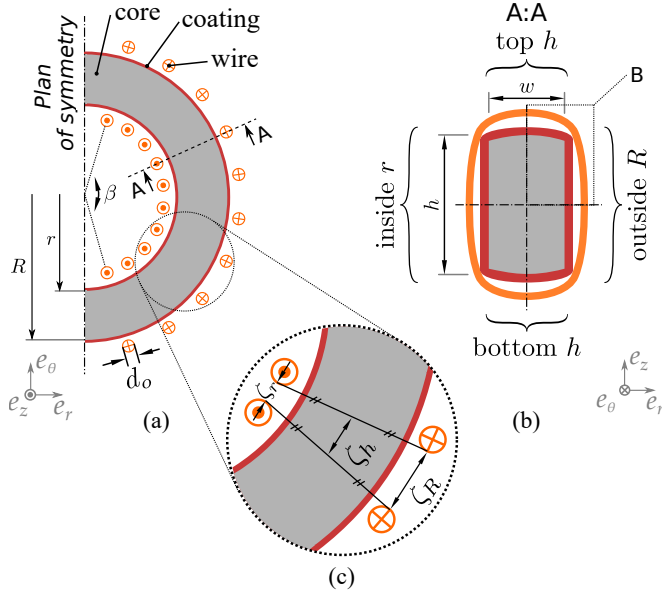


Fig. 3. Description of the geometry of the component: (a) half transversal cut of the component, (b) section cut A:A with close-up B of a quarter of the section, and (c) close-up of a pair of turns.

### B. Preparation of the geometry for 2D FEM simulations

1) *Geometry of the wound component:* Fig. 3 shows the geometry of the wound component with one winding. The half transversal cut of the core depicted in Fig. 3(a) presents the internal and external radius, respectively  $r$  and  $R$ , and the winding angle  $\beta$  covered by the  $N$  regularly spaced turns. The core section is defined by its width  $w$  and its height  $h$  as shown in Fig. 3(b). The close-up B on one quarter of the section is presented later in Fig. 4. The distances between two adjacent turns are presented in Fig. 3 in the close-up (c) with  $\zeta_r, \zeta_R$  the mean inter-turn distances respectively on the internal and external surface of the core, and  $\zeta_h$  the mean inter-turn distance on the top and bottom surfaces. In order to compute the capacitances  $C_{tc}, C_{tt}$  and  $C_f$  with a 2D FEM approach, the presented geometry will be transformed. The retained hypotheses are described in details hereafter.

2) *Focus on one face of the component:* Fig. 4(a) presents a quarter of the section of the component along with the measured dimensions. The core dimensions  $h$  and  $w$  are given by the datasheet from the manufacturer. The coated dimensions  $h_c, w_c$  are measured at the middle of each face using a caliper. And the same is performed for the dimensions of the wound component  $h_t$  and  $w_t$ . The wire is assumed to touch the coated core on a small surface on the corner, at a distance  $e$  from the core corner due to coating, with relative permittivity  $\epsilon_c$ . The impact of the corner is first neglected in this section. The area delimited by the edge of the iron surface and the position where the wire comes off the coated surface is considered for the following transformations, as depicted in Fig. 4(b). The maximum turn-core space  $s$  and coating thickness  $c$  are deduced from the previous measurements. The inter-turn spaces, presented earlier in Fig. 3(c), are deduced from the measurements of the winding angle  $\beta$ , the geometry of the

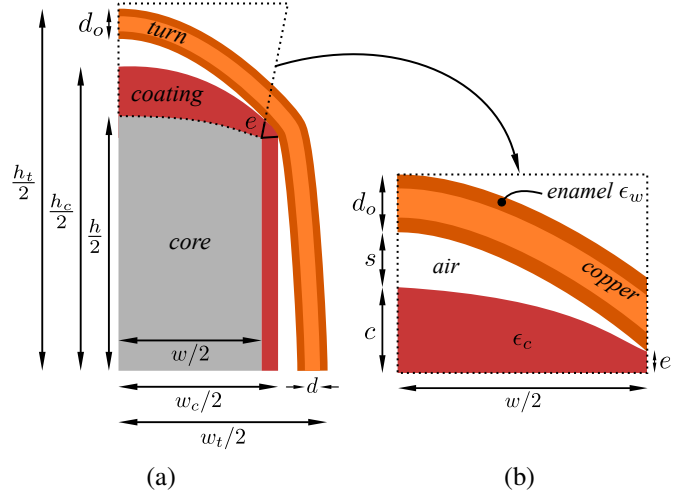


Fig. 4. Close-up on a quarter of section: (a) Quarter of section B from Fig. 3(b) with measured dimensions, (b) details of the top face from the core surface with deduced dimensions.

wound core  $R_t, r_t$ , the number of turns  $N$ , and the insulated wire diameter  $d_o$  as presented in (4)

$$\begin{cases} \zeta_R &= \frac{\beta}{N-1}(R_t + d_o/2) - d_o \\ \zeta_r &= \frac{\beta}{N-1}(r_t - d_o/2) - d_o \\ \zeta_h &= \frac{1}{2}(\zeta_R + \zeta_r) \end{cases} \quad (4)$$

3) *Compensation of the wire insulation:* The wire insulation is a thin layer of enamel (30  $\mu\text{m}$ , or 6% of the wire copper diameter in our experiments) that requires a fine meshing in FEM simulation. A transformation of the conductor diameter is proposed to decrease the number of domains and elements and speed up the simulation time for optimization purpose. The Fig. 5(a) depicts a cross section of a pair of turns wound around the core, with  $d$  the copper diameter of the wire,  $e_w$  the insulation thickness and  $\epsilon_w$  its relative permittivity. Given the small size of the wire diameter compared to the core radius, the curvature of the core is neglected. Considering the thinness of wire insulation layer, it can be assumed that electric field lines remain orthogonal to the enamel surfaces, such that the elementary capacitance of wire insulation  $dC_w$  (in series with the air one  $dC_a$ ) can be replaced by  $dC_{wc}$  made of air and of a smaller thickness in such way that  $dC_w = dC_{wc}$ , as demonstrated in Fig. 5(b). This leads to an equivalent wire without insulation, where copper diameter  $d$  is increased by two times the additional length  $\delta_w$ . That gives corrected values of diameter  $d_c$ , inter-turn space  $\zeta_c$ , turn-core space  $s_c$ , and turn-core distance at the edge  $s_e$  as presented in (5) and shown in Fig. 6.

$$\begin{cases} \delta_w &= e_w \cdot \left(1 - \frac{1}{\epsilon_w}\right) \\ d_c &= d + 2\delta_w \\ \zeta_c &= \zeta + 2\frac{e_w}{\epsilon_w} \\ s_c &= s + \frac{e_w}{\epsilon_w} \\ s_e &= \frac{e_w}{\epsilon_w} \end{cases} \quad (5)$$

4) *Flattening of the turn and coating curvatures:* The thickness of the coating is not constant, and each turn follows

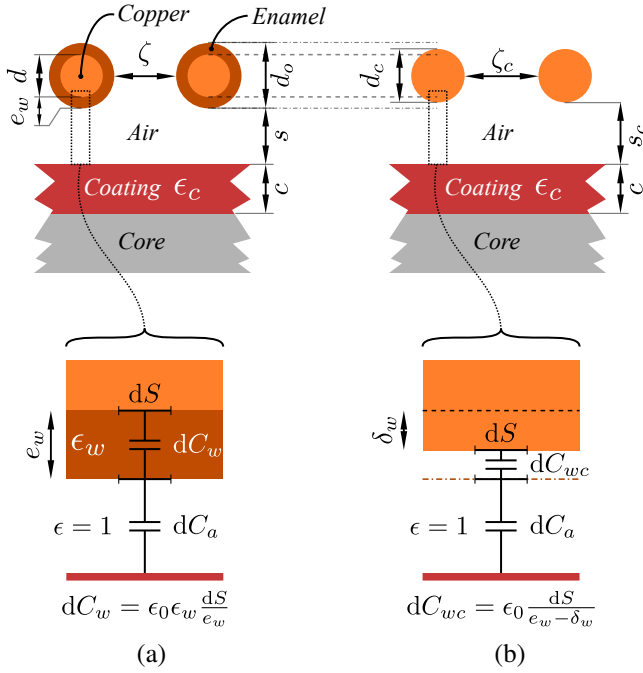


Fig. 5. Equivalent model of the wire insulation: (a) before and (b) after the compensation of the insulation layer is applied.

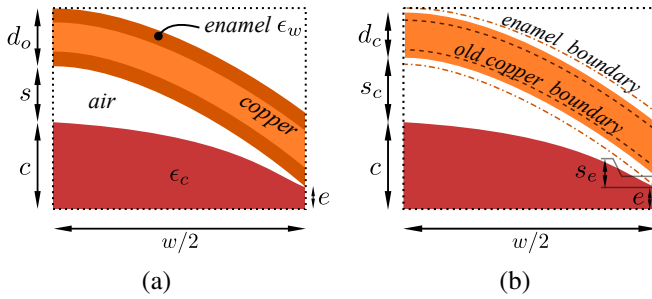


Fig. 6. Diagram of the top surface of the component with the compensation of wire enamel.

a curve as presented in Fig. 7(a). To simulate the parasitic capacitances in 2D FEM, every distance of interest must be constant along the face considered as shown in Fig. 7(b). Thus, the capacitive behavior of the curved wire and coating over the considered width is modeled as series capacitances  $C_{air}$  and  $C_{coat}$  between flattened surfaces. Taking only the maximum distances  $s_c$  and  $c$  is a first order approximation of the turn-core distance and coating thickness. But it will lead to an underestimation of the capacitances as shown in the next section. A better approximation that conserves the value of the capacitances is proposed in the following paragraph, with a focus on  $C_{air}$ .

As a geometrical model of the curvature, the turn-coating distance is assumed to follow a parabola  $S$  as defined in (6) and shown in Fig. 8(a). Assuming that  $(s_c - s_e) \ll w/2$ , a straight elementary capacitance per unit area  $dC$  is defined along a portion  $dx$  of the length  $w/2$ . One can express the average capacitance per unit area over the full width as in (7). By equalizing it to a constant capacitance per unit area defined between two straight surfaces, an equivalent turn-

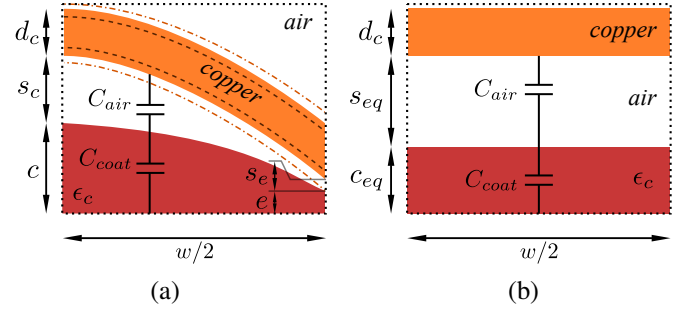


Fig. 7. Diagram of the top surface of the component (a) before and (b) after flattening.

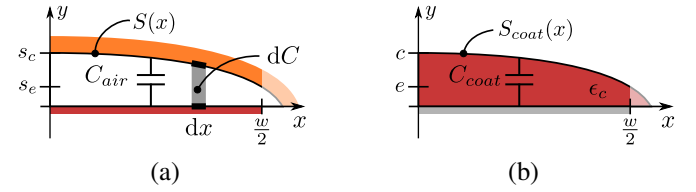


Fig. 8. Diagrams of the flattening of (a) the wire curvature, and (b) the coating curvature.

coating distance that gives the same overall capacitance value  $C_{air}$  is extracted. This distance, called  $s_{eq}$ , is retrieved from (7) and presented in (8). If the coating thickness is not constant on the considered face, as presented in Fig. 7(a) for the top face, the same approach is used by defining a second parabola  $S_{coat}$  as in Fig. 8(b) and obtaining an equivalent thickness  $c_{eq}$  by applying (8).

$$S(x) = s_c - (s_c - s_e) \cdot \frac{x^2}{(w/2)^2} \quad (6)$$

$$\frac{2}{w} \int dC = \frac{2}{w} \int_0^{w/2} \frac{\epsilon_0}{S(x)} dx = \frac{\epsilon_0}{s_{eq}} \quad (7)$$

$$s_{eq} = \frac{2\sqrt{s_c \cdot (s_c - s_e)}}{\log \left( \frac{\sqrt{s_c} + \sqrt{s_c - s_e}}{\sqrt{s_c} - \sqrt{s_c - s_e}} \right)} \quad (8)$$

Once all the previous transformations have been applied on each face, the geometry is ready for the 2D FEM simulations of the parasitic capacitances  $C_{tc}$ ,  $C_{tt}$  and  $C_f$  along the considered face.

### C. Simulations of the elementary parasitic capacitances

The simulation setups of  $C_{tc}$ ,  $C_{tt}$  and  $C_f$  are described in Fig. 9, they are all planar simulation of the same depth (depending on the simulated face, for example  $h$  for the inside face), computed thanks to *FEMM 4.2* [33]. The margin with the bounding box  $h_{box}$  and  $w_{box}$  are defined as ten times the characteristic distance of the setup (the maximum between the inter-turn and turn-core distances) to avoid strong coupling with the boundaries. Periodic boundary are used for Fig. 9(a) to avoid coupling with the boundary as shown by the mirror setup. Anti-periodic boundaries are used in Fig. 9(b) for the same reason. For each sub-figure (a), (b)



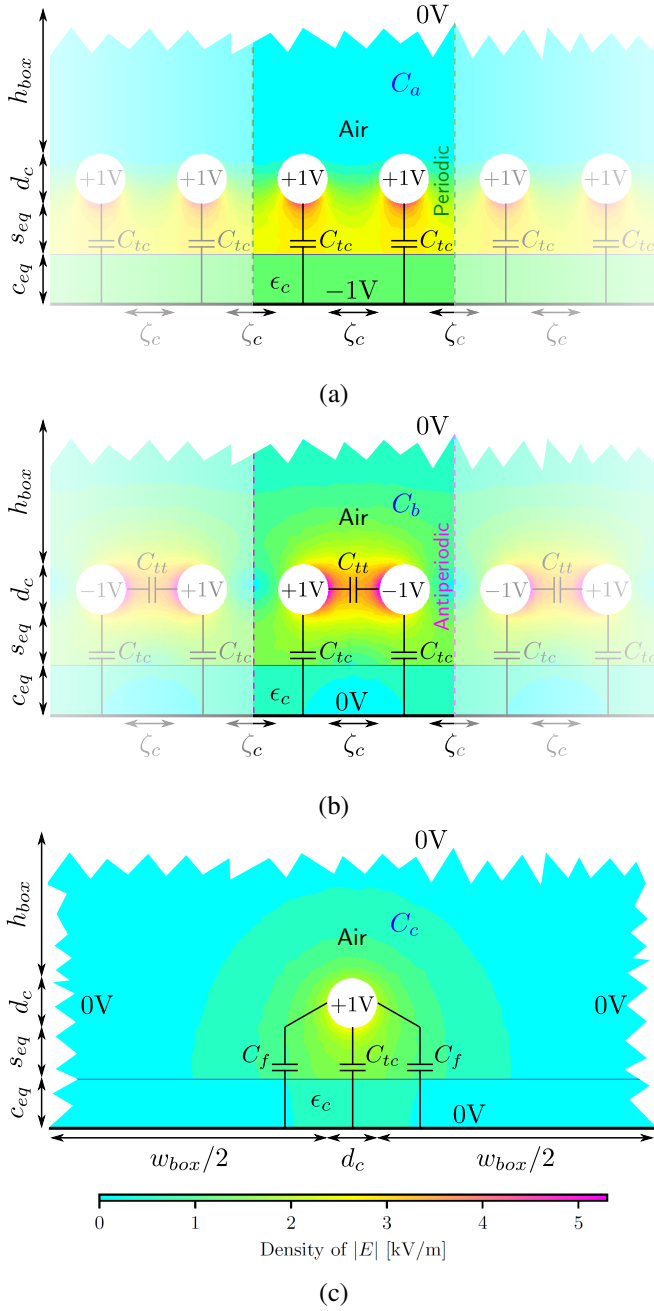


Fig. 9. Electric field map and their equivalent capacitances network for a pair of turn : (a)  $C_a$  for  $C_{tc}$  extraction, (b)  $C_b$  for  $C_{tt}$  extraction, (c)  $C_c$  for  $C_f$  extraction, the torn edges indicate that the simulation domain extends far beyond them.

and (c) of Fig. 9, the respective total capacitances  $C_a$ ,  $C_b$  and  $C_c$  are retrieved from the total energy. Then the elementary capacitance of interest  $C_{tc}$ ,  $C_{tt}$ ,  $C_f$  are computed thanks to (9). This process is applied to each face of the core along the cross-section shown in Fig. 3(b), involving a first set of elementary capacitances identified by the  $R$  subscript ( $C_{tcR}$ ,  $C_{ttR}$ ,  $C_{fR}$ ) for the outside face, a second set  $C_{kr}$  for the inside face, and  $C_{kh}$  for both the top and bottom faces. Finally, totalized elementary capacitances are obtained by summing the results from each face as shown in (10).

TABLE I  
INTER-TURNS AND TURN-CORE SPACES FOR DIFFERENT WINDING CASES.

|              | Cases |               |                |       |
|--------------|-------|---------------|----------------|-------|
|              | Tight | Loose $\zeta$ | Loose $s_{eq}$ | Loose |
| $\zeta$ [mm] | 0.1   | 1.0           | 0.1            | 1.0   |
| $s$ [mm]     | 0.1   | 0.1           | 1.0            | 1.0   |
| Drawing      |       |               |                |       |

$$\begin{cases} C_{tc} = \frac{C_a}{2} \\ C_{tt} = C_b - \frac{C_{tc}}{2} \\ C_f = \frac{C_c - C_{tc}}{2} \end{cases} \quad (9)$$

$$\forall k \in \{tc, tt, f\}, C_k = C_{kR} + C_{kr} + 2 \cdot C_{kh} \quad (10)$$

In comparison to analytical formulations in the literature [18]–[22], the enamel insulation layer is taken into account, in addition to the coating of the core. Furthermore, the 2D FEM setups are easier to implement and faster to compute than a full 3D model of the component. The relevance of this method is further discussed in the following based on comparisons with non-FEM approaches.

#### D. Comparison of methods for determining elementary capacitances

The FEM simulations presented in the previous subsection for determining the elementary capacitances  $C_{tc}$  and  $C_{tt}$  are compared with analytical methods from the literature [18], [22]. The method described in [22], takes into account coating layer of the core and insulation layer of the wire, in addition to inter-turn and turn-core spaces. So this work is directly comparable to the proposed approach. On the contrary, the method described in [18] uses the image theory method, but with the assumption of no insulation layers on the conductor and on the core, and the authors make no recommendations about how to take them into account. In order to make a fair comparison, three hypotheses will be used hereafter. The simplest ones are to replace any insulation layer with either air or conductor as described respectively in (11) and in (13). The more realistic one, called *intermediate*, is to replace only a part of insulation layer by conductor and the other part by air by using parallel plate capacitor approximation, as proposed in Fig. 5 and specified in (12). The methods are tested on four winding cases derived from the geometry presented in Fig. 9 and described in Table I, while the remaining parameters are kept constant:  $d = 0.5$  mm,  $d_w = 0.56$  mm,  $\epsilon_w = 4$ ,  $c_{eq} = 0.2$  mm,  $\epsilon_c = 3$ .

$$\begin{cases} d_{c,air} = d \\ s_{eq,air} = s_{eq} + e_w + c \\ \zeta_{c,air} = \zeta + 2 \cdot e_w \end{cases} \quad (11)$$

$$\begin{cases} d_{c,inter} = d_c \\ s_{eq,inter} = s_{eq} + \frac{e_w}{\epsilon_w} + \frac{c}{\epsilon_c} \\ \zeta_{c,inter} = \zeta_c \end{cases} \quad (12)$$

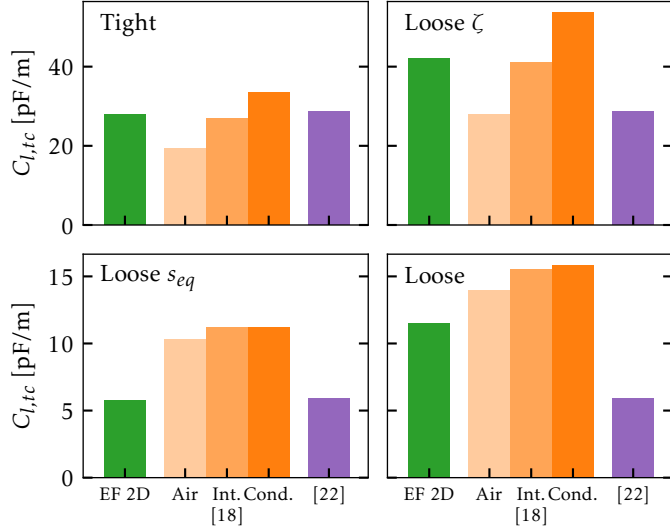


Fig. 10. Comparison of the analytical methods for determining  $C_{l,tc}$  capacitances for each case to the proposed 2D FEM approach.

$$\begin{cases} d_{c,cond} &= d_w \\ s_{eq,cond} &= s_{eq} \\ \zeta_{c,cond} &= \zeta \end{cases} \quad (13)$$

In this subsection, the methods are compared assuming that the 2D hypotheses to take into account curvatures of wire are the same and have been applied to all the methods. The relevance of these hypotheses will be discussed in the next section. Only the turn-core capacitance is studied because  $EPC$  is more sensitive to it according to (3).

The breakdown of the results for the linear turn-core capacitance  $C_{l,tc}$  for each case and for each method from the literature are shown in the Fig. 10. For [22] there are some cases that results in the same value, for example  $C_{l,tc}$  both *Tight* and *Loose*  $\zeta$  are identical. However that is expected since the method that computes  $C_{l,tc}$  is independent from  $\zeta$ . According to these results [22] performs with a relative error of less than  $\pm 3\%$  for cases with small  $\zeta$  compared to  $d$ . When adjacent turns are far away from each other in comparison to  $d$  the method gives only an order of magnitude and underestimates the value by at least 30%.

For [18], and for both cases *Tight* and *Loose*  $\zeta$ , the hypothesis regarding the insulation layers that leads to the best results is the *intermediate* one, with a relative error of less than  $\pm 10\%$ . For the last *Loose* cases with  $\zeta$  big compared to  $d$ , the method always overestimates  $C_{l,tc}$ .

This study shows that both analytical methods for determining the elementary capacitances [18], [22] are good compared to the proposed FEM method (relative errors less than  $\pm 5\%$ ) for the *Tight* winding only, and by considering specific hypotheses for the insulation layers with [18]. Yet, this paper aims at a general method also suitable for *Loose* winding in the aim of  $EPC$  reduction in section V. Thus, the proposed FEM method is applied hereafter for determining  $C_{tc}$  and  $C_{tt}$ . The accuracy of the method will be discussed with measurements of  $EPC$  in the following sections, based

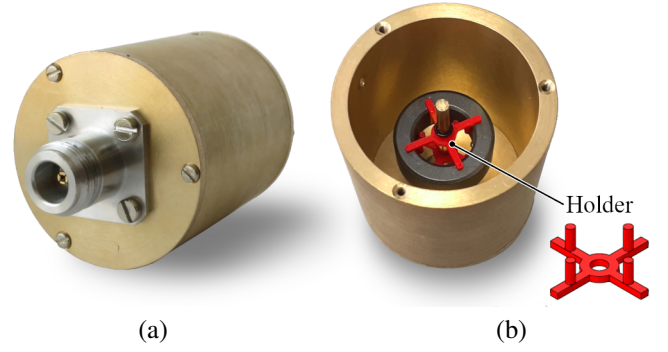


Fig. 11. Photographies of the one-turn equivalent brass device for the characterization of magnetic ring cores : (a) outside, (b) inside with a loaded core. The red crosses are 3D printed plastic holders for the core.

on two ring cores from different suppliers and different kind of materials.

### III. APPLICATION TO CONDUCTIVE MAGNETIC MATERIAL

To validate the obtained model, a coated ring core called Device Under Test 1 (DUT1) is chosen (*Vacuumschmelze: T60004-L2030 W911*). This core is made of nanocrystalline material that is a good conductor and fulfills the perfect conductor hypothesis. It is wound by hand with one winding made of copper wire of diameter 0.5 mm with an enamelled insulation layer of thickness 30 m and relative permittivity of 4 (at 1 MHz, 60 °C according to [34]).

#### A. EPC measurements

To extract the  $EPC$  of a wound DUT, two measurements of complex impedance versus frequency  $f$  are performed.

The first one is done with a single-turn winding, called  $Z_{N1}$ , to characterize the core without parasitics and to obtain the ideal impedance of the choke without the  $EPC$ , called  $Z_{ideal}$ , as in (14). To perform such measurements a one-turn equivalent device has been designed and made of brass as depicted in Fig. 11. The core is maintained centered on the axis by a 3D printed device in thermoplastic *Poly-Lactic Acid* (PLA) called holder in the Fig. 11(b). The self-impedance of the device without a core is subtracted from the measured impedance with the DUT inside it to retrieve the characteristic impedance of the core  $Z_{N1}$ . Parasitic capacitances of the core with the device are negligible for the cores studied here. The remaining parasitic capacitance of the device at no load has been cancelled out by the OPEN compensation of the impedance.

The second one is performed with the winding,  $Z_{meas}$ , to deduce the value of  $EPC$ . Indeed, the  $EPC$  is extracted by fitting the model impedance  $Z_{mod}$ , that results from the paralleling of  $Z_{ideal}$  and  $EPC$  presented in (15), to the measured one  $Z_{meas}$ , with  $EPC$  as the design variable. This way the possible dispersion of the relative permeability among the samples, and its decrease with high frequency do not impact the extracted  $EPC$  value of one specific core. The impedance measurements are carried out with an impedance analyser *HP4294A* equipped with the socket *16047E*. A space

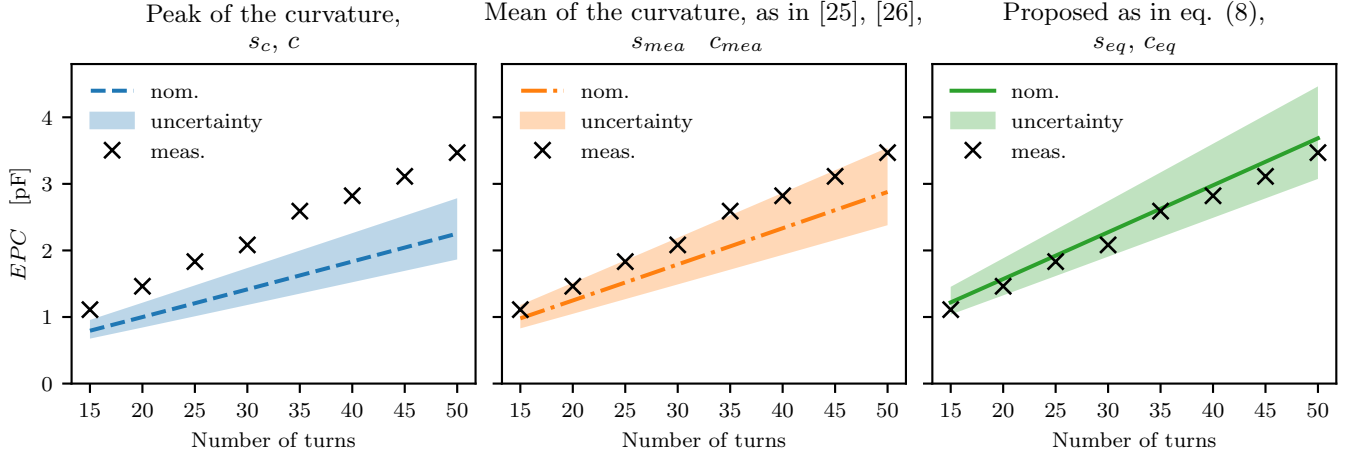


Fig. 12. Evolution of the EPC against the number of turns for the nanocrystalline core DUT1 with one winding: comparison of the three hypotheses for the computation of the turn-core spaces  $s_{eq}$  and coating thickness  $c_{eq}$  regarding their curvature, with worst cases min-max.

of 2 cm between the DUT and the socket is ensured to avoid direct coupling of the winding with the socket. According to the datasheets of the *HP4294A* and the *16047E* the relative error on the impedance module  $\delta_Z$  in the frequency range of the fitting (10 kHz to 20MHz) is less than  $\pm 3\%$ . This leads to a similar maximum relative error  $\delta_{EPC} = -\delta_Z / (1 + \delta_Z)$  on the extracted *EPC* of approximately  $\pm 3\%$ .

$$Z_{ideal}(f) = N^2 Z_{N1}(f) \quad (14)$$

$$Z_{mod}(f) = \frac{N^2 Z_{N1}(f)}{1 + j \cdot 2\pi f \cdot EPC \cdot N^2 Z_{N1}(f)}. \quad (15)$$

### B. Validation on impedance measurements

To apply the model to the DUT1, its geometry is measured before and after winding with a caliper. The coating thickness is deduced from the subtraction of the datasheet dimensions from the coated core measurements. Since the winding has some irregularities, each distance is measured at several angles on the component. In addition to the nominal case, two worst cases are computed to provide an interval of the modelled value due to uncertainties. The minimal case is defined by the maximum turn-core compensated distances  $s_c$ , maximum coating thicknesses  $c$ , and minimal coating relative permittivity. The opposite is performed to obtain the maximum case. Since the model considers only regular winding distribution, the worst cases give an overestimation of the interval around the nominal value. The resulted EPC is compared to the measured one in Fig. 12, for several hypotheses regarding the 2D approximation of the turn and thickness curvature: the maximum distances  $s_c$  and  $c$ , the mean distance under the core and thickness on the top and bottom of the core as proposed in [25], [26], and the inverse of the mean inverse distances  $s_{eq}$  and  $c_{eq}$  according to (7) and (8). For the three hypothesis the evolution of EPC with number of turns has the correct trend. This justifies the use in the three cases of the energetic approach to solve the capacitive network. The value of the EPC when using  $s_c$  underestimates the measured value by more than 30% for the nominal case, and the maximum

value is below the measurement by 20%. It means that this hypothesis is not correct for the modelling of the EPC. The use of  $s_{mean}$  and  $c_{mean}$  gives better results. Indeed the relative error compared to the measurements is below 20%, and some measurements points are encompassed in the min-max area, though they remain near the upper bound of the interval. The last one that uses (8) as  $s_{eq}$  performs better than the previous one: its relative error for the nominal case is only 6% in average. This means that the model is able to give both the correct value and its evolution over the number of turns. Introducing the min-max cases, the model value is comprised in an interval of  $-15\%$  to  $+30\%$ . As a consequence even with some imperfections and uncertainties the correct order of magnitude of the EPC is given by the proposed model. These measurements validate the 2D hypotheses described earlier, and the energetic approach used to solve the capacitive network. The comparison of the impedances in Fig. 13 shows that the proposed EPC model allows to extend the frequency range of the modelled impedance up to 20MHz in this specific case.

## IV. APPLICATION TO HIGH PERMITTIVITY MN-ZN MATERIAL

The validity of the model regarding the hypothesis on the electric behaviour of the magnetic material is studied for Mn-Zn ferrite materials commonly used in EMI filter design.

### A. Characterization of the dielectric behaviour of the magnetic material

The model is applicable on all material that can be considered as a perfect conductor and on all material with a high permittivity, because it would cause a negligible voltage drop along the core. To verify this assumption, a simple and non destructive test is performed on two cores of similar geometry and of different material, Mn-Zn N30 and Ni-Zn 4F1. The proposed capacitive measurement will give an estimation of the dielectric properties of the core and its coating, and will help to decide whether the model is applicable or not on this

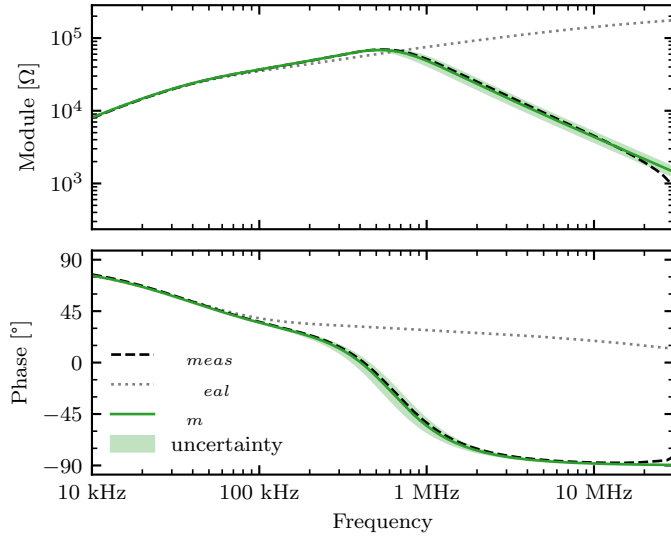


Fig. 13. Comparison of the measured and modelled impedance of the DUT1 with 50 turns.

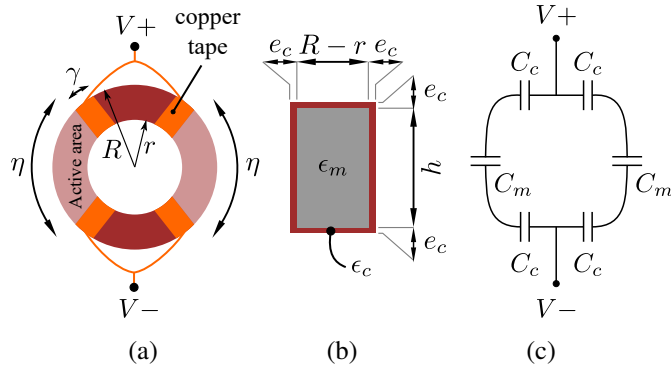


Fig. 14. Non destructive test of the core relative permittivity  $\epsilon_m$ : (a) drawing of the core equipped with copper tape electrodes, (b) section of the coated core, (c) equivalent capacitive network.

material. In Fig. 14(a), copper tape of width  $\gamma$  (here 5 mm) is used to build surface electrodes on the coated core, separated by an angle  $\eta$  and symmetrically duplicated in two branches such that only the portions of the core comprised within the  $\eta$  angles undergo electrostatic excitation, called *active area*. Thus, the electric flux goes from one pair of electrode ( $V+$ ) through a first layer of coating, then the core, and finally a second layer of coating to the other pair of electrodes ( $V-$ ). An equivalent capacitive network of the measurement is shown in Fig. 14(c) with  $C_c$  the capacitance through the coating under one electrode, and  $C_m$  the capacitance through the magnetic material. According to the diagram of the section of the core, shown in Fig. 14(b), the coating capacitance can be estimated as in (16) with  $e_c$  the mean thickness of coating. The material capacitance is assimilated to a plane capacitance in the active area as in (17). The resulting overall capacitance  $C_{eq}$  is expressed in (18).

$$C_c = \frac{\epsilon_0 \epsilon_c 2(R - r + h)\gamma}{e_c} \quad (16)$$

$$C_m = \frac{\epsilon_0 \epsilon_m (R - r)h}{\eta \cdot \frac{R+r}{2}} \quad (17)$$

$$C_{eq} = \frac{2C_m C_c}{C_c + 2C_m} \quad (18)$$

Since  $C_m$  and  $C_c$  capacitances are in series, if the core permittivity  $\epsilon_m$  is high so that  $C_m \gg C_c$ , then the voltage drop in the core remains negligible and  $C_{eq} \approx C_c$  whatever the inter-electrode angle  $\eta$ . On the other hand, if low  $\epsilon_m$  brings  $C_m$  to a comparable or lower value than  $C_c$ , then increasing  $\eta$  should reduce  $C_{eq}$  in (18) as a result of lower  $C_m$  in (17). Thus, Fig. 15 presents  $C_{eq}$  capacitance measurements for different angles on the two core materials: DUT2 (Mn-Zn N30 of reference B64290L0632X830) and DUT3 (Ni-Zn 4F1 of reference TX20/10/7). In addition,  $C_c$  is estimated at 15.3 pF from (16) (using  $\epsilon_c = 3$  and  $e_c = 125 \mu\text{m}$  from the measurements), so that the trend of  $C_{eq}$  is also plotted for different  $\epsilon_m$  values. According to the localisation of the measurement points in Fig. 15, it can be concluded that on one hand the Mn-Zn material N30 has a high relative permittivity and the proposed model of the EPC can be readily applied, while on the other hand the Ni-Zn material 4F1 has a low permittivity and the model is not applicable. Thus, the test setup proposed in this section allows simple evaluation of the model applicability to a given ferrite core.

#### B. Experimental validation with impedance measurements

DUT4 is a Mn-Zn N30 core of reference B64290L0618X830, and of similar size to DUT1. Direct application of the proposed model to this high-permittivity ferrite material is confirmed by the comparison of the extracted and measured EPC on the wound DUT4 as presented in Fig. 16. The evolution and the order of magnitude of the EPC is correctly reproduced, the average relative error to the measurement is 20%. It should be noted that the geometry of the core DUT4 is slightly different than DUT1. The top and bottom sides are more bumpy. This could account for the bigger relative error than for DUT1.

### V. REDUCTION OF THE EPC

The validated model to extract the EPC is used here to propose actions to reduce its value. According to (3) the main contributor is  $C_{tc}$ . To minimize its value, two methods can be used: one based on the inter-turn spacing, the other on the turn-core spacing. For this section the same core reference as DUT1 is used but with two windings to validate the model for common-mode inductors at the same time.

#### A. Small inter-turn spacing

According to 2D FEM simulations (setups described in Fig. 9) performed on the inside face of the component for different values of  $s_r$  and  $\zeta_r$ , and presented in Fig. 17, the inter-turn space  $\zeta$  should be kept as small as possible to minimize  $C_{tc}$ . Indeed the electrical field lines can reach more surface of the core when two adjacent turns are far apart each other. Since keeping the winding tight is already performed on regular components to increase their power density, this design rule does not compete with existing ones.



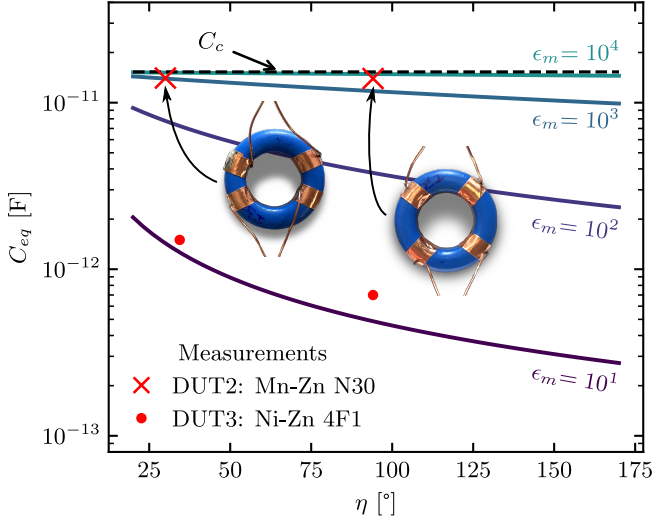


Fig. 15. Evolution of the equivalent capacitance as a function of core relative permittivity  $\epsilon_m$  and angle  $\eta$  between electrodes.

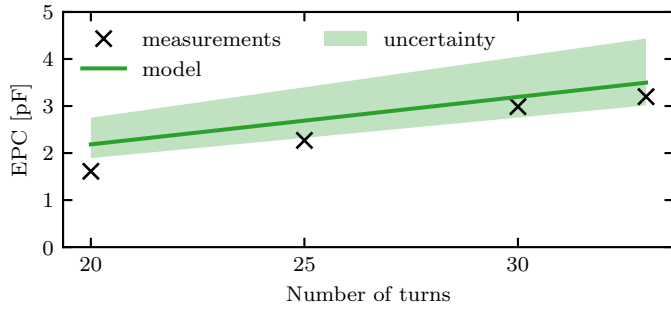


Fig. 16. Evolution of the EPC against the number of turns for one winding for the Mn-Zn core DUT4.

### B. Increase of the turn-core spacing

As depicted in Fig. 17,  $C_{tc}$  is also inversely proportional to the turn-core spacing  $s$ . Thus specific devices called *spacers* are proposed to increase this space on all the faces of the component.

1) *Design of the spacers*: The spacers are designed to increase the turn-core spaces while adding a minimum of dielectric material, thanks to their placement on the corners of the section. They are made of three parts built by additive manufacturing with PLA material, and glued together. Three wound components are shown in Fig. 18(a): one without

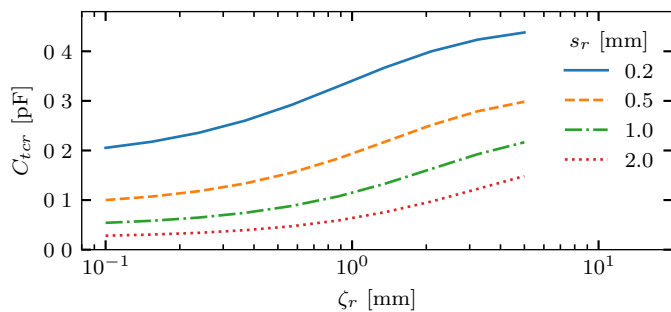


Fig. 17. Evolution of  $C_{tc}$  as a function of  $s_r$  and  $\zeta_r$ .

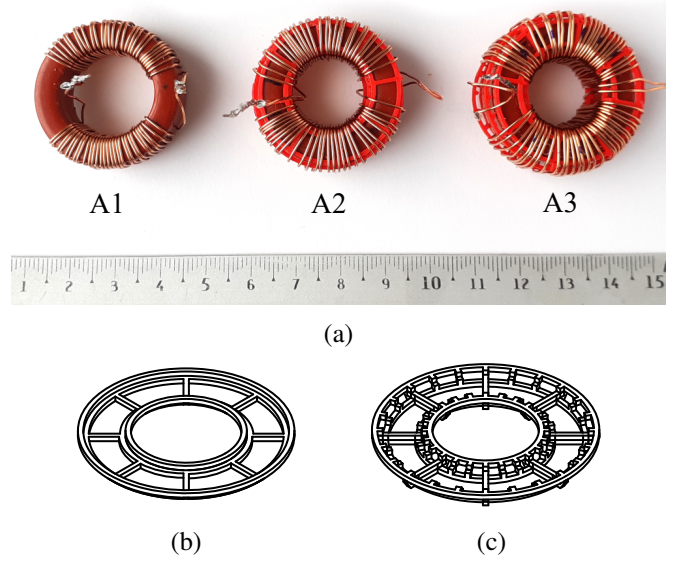


Fig. 18. Wound components series with different turn-core space: (a) photograph of A1 without spacers, A2 and A3 equipped with spacers of thickness 0.8 mm shown in drawing (b), and of thickness 1.6 mm shown in drawing (c), respectively.

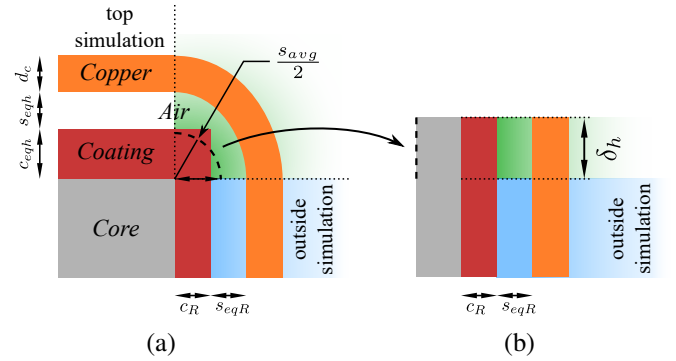


Fig. 19. Drawings of (a) the outside top corner of a turn, and (b) its 2D transformation.

spacer (named A1) and two others (A2 and A3) equipped with spacers shown in Fig. 18(b) with thickness 0.8 mm and (c) with thickness 1.6 mm, respectively.

2) *Taking into account the corners in the model*: Fig. 19(a) shows a close-up view of the corners of a turn, which were not taken into account so far. However, as the turn-core distance is increased, their contribution to overall  $C_{tc}$  may not be neglected. Thus, this small part is taken into account by increasing the domain simulation of the inside and outside faces, as depicted in Fig. 19(b). The increase  $\delta_h$  of the height  $h$  for the simulation, on the outside of the core, is equal to the path of the mean space under the corner  $s_{avg}$  as defined in (19) and as presented in Fig. 19(b). This is repeated on the other corner on the same side, and on the two inside corners of the core. This new hypothesis is added to the model and the resulting model is called extended model.

$$\delta_h = \frac{\pi}{2} \frac{s_{avg}}{2} = \frac{\pi}{4} \frac{s_{eqR} + c_R + s_{eqh} + c_{eqh}}{2} \quad (19)$$

3) *Experimental validation:* The Fig. 20 shows the measured and modelled values of the EPC as a function of the spacer thickness  $e_s$ . To compute the modelled values the following theoretical values have been applied to all faces: a constant space  $e_s$  on all the faces of the component, a maximum turn-core distance  $s$  defined as in (20) from empirical observations, and inter-turn distances  $\zeta$  computed accordingly with (4) and estimated  $R_t$  and  $r_t$ .

$$s = e_s + \frac{2}{3}d_o \quad (20)$$

As expected the EPC decreases with bigger  $e_s$ . For instance, between A1 and A3 designs, the EPC has been reduced by 73%, while the cylinder volume of the wound component has been increased by 54% between A1 and A3 designs. It is worth pointing out that between A1 and A2 designs the decrease on the EPC is still significant (65%) while the impact on the volume is only +37%. This behaviour is explained by the fact that  $C_{tc}$  is approximately inversely proportional to  $e_s$ . This means that with a small increase in  $e_s$  the EPC will drop fast, with low volume penalty. This is emphasized in Fig. 21 where an area of low increase in volume and high decrease of EPC has been highlighted. In Fig. 20, the underestimation of the models to the measured value are at maximum 26.8% and 17.5% respectively for the base model and the extended one. This demonstrates that the corners play a relatively bigger role in the case of larger  $e_s$ . But the overall underestimation of EPC with both models shows that a discrimination of each face of the components and a precise knowledge of each distance on each face may be necessary to further improve accuracy. This is confirmed by the application of the extended model to the measured devices called *ext. model corr.* in Fig. 20, for which the relative error is reduced between -10% and 12.8%. The overestimation for A1 is consistent with previous results, and the underestimation for A2 and A3 might be due to the neglected PLA material of the spacers (such dielectric has relative permittivity of around 3 at the considered frequencies according to [35]), which represent roughly 20% of the perimeter of the section of DUT1. Nevertheless, even without the correction, the proposed model is able to give a robust and precise order of magnitude of the EPC as a function of the turn-core space, which can be beneficial to anticipate the high-frequency response of a coupled inductor at the design stage.

Finally, it has been checked that the differential mode inductance (leakage inductance) of the common mode chokes does not increase with bigger turn-core spaces. It has even decreased of roughly 25% compared to tight case A1 because of the increase of the angle covered by the windings. This behaviour is confirmed and explained by [36].

## VI. CONCLUSION

A model of the equivalent parallel capacitance of inductors due to parasitic capacitances of the winding has been developed. The proposed 2D FEM model is applicable to coated ring core, with one winding or two excited in common-mode, and is robust even for determining the elementary capacitances for loose windings. In addition to the classical

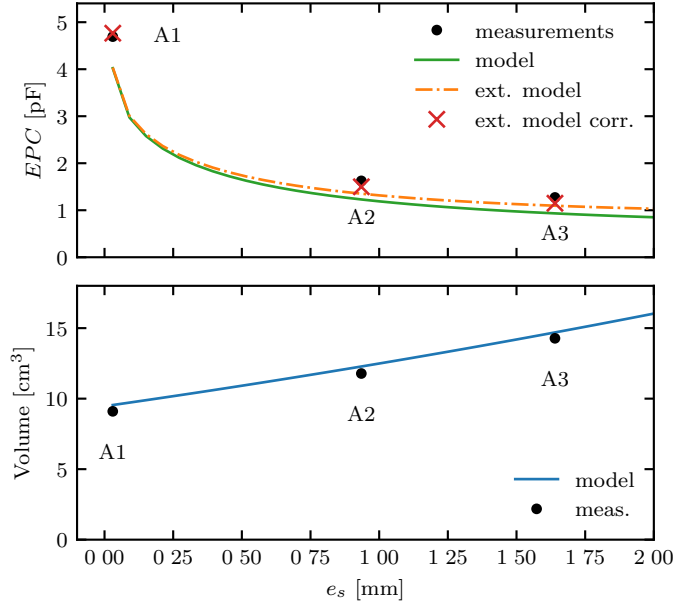


Fig. 20. Evolution of the EPC and cylinder volume against the spacer thickness  $e_s$ .

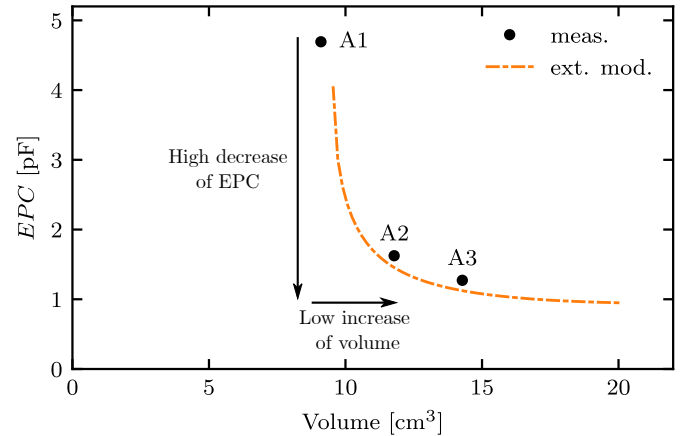


Fig. 21. Evolution of the EPC against the cylinder volume.

inter-turn and turn-core capacitances, the contribution of the fringe and of the corner capacitances have been integrated into the model. It is valid for magnetic material that can be considered as perfect conductor or with a high permittivity. In addition, a simple non destructive test has been proposed to help designers to determine whether the model is applicable or not to a specific magnetic material. The model gives the value of the EPC as a function of the number of turns with a satisfactory relative error of 15%, even for loose windings, thanks to accurate 2D transformation of the curved turns and coating thickness. The assumption used was compared to simpler assumptions and found to be better. The model has been validated for different design parameters including turn-core space, allowing to propose a solution for the fine tuning and reduction of the EPC as a trade-off with the total volume of the component. Hence plastic spacers are used to increase the turn-core distance and thus decrease the EPC. The perspectives of this work concern the extension of the

proposed model regarding low permittivity magnetic material like Ni-Zn and its application to EMI filters optimization. Indeed for magnetic material with low permittivity the perfect conductor hypothesis might not hold and some revisions of the parasitic capacitances model are needed. To use the model as a fully predictive tool of the EPC, a model for the turn-core distance  $s$  as a function of the core geometry, the diameter of the wire, and the mechanical tension applied on the wire during the winding should be derived. Other winding shapes are also a perspective of this work. The case where turns are kept close to the core thanks to plastic ties for cores with a big height compared to their radius, is a good example. A loss and thermal models of the component are also desirable to study the thermal advantages and drawbacks of the proposed solution to reduce the EPC, based on loose winding. Finally the proposed model will be used in the optimization of the volume of the inductor under the constraints of the EMC standards for high frequency power converters.

## REFERENCES

- [1] A. K. Morya, M. C. Gardner, B. Anvari, L. Liu, A. G. Yepes, J. Doval-Gandoy, and H. A. Toliyat, "Wide bandgap devices in AC electric drives: Opportunities and challenges," *IEEE Transactions on Transportation Electrification*, vol. 5, no. 1, pp. 3–20, 2019.
- [2] B. Zhang and S. Wang, "A survey of EMI research in power electronics systems with wide-bandgap semiconductor devices," *IEEE Journal of Emerging and Selected Topics in Power Electronics*, vol. 8, no. 1, pp. 626–643, 2020.
- [3] K. Mainali and R. Oruganti, "Conducted EMI mitigation techniques for switch-mode power converters: A survey," *IEEE Transactions on Power Electronics*, vol. 25, no. 9, pp. 2344–2356, 2010.
- [4] B. Zaidi, A. Videt, and N. Idir, "Optimization method of CM inductor volume taking into account the magnetic core saturation issues," *IEEE Transactions on Power Electronics*, vol. 34, no. 5, pp. 4279–4291, 2019.
- [5] S. Wang, F. Lee, D. Chen, and W. Odendaal, "Effects of parasitic parameters on EMI filter performance," *IEEE Transactions on Power Electronics*, vol. 19, no. 3, pp. 869–877, 2004.
- [6] M. Hartmann, H. Ertl, and J. W. Kolar, "EMI filter design for a 1 MHz, 10 kW three-phase/level PWM rectifier," *IEEE Transactions on Power Electronics*, vol. 26, no. 4, pp. 1192–1204, 2011.
- [7] X. Huang, J. Feng, F. C. Lee, Q. Li, and Y. Yang, "Conducted EMI analysis and filter design for MHz active clamp flyback front-end converter," in *2016 IEEE Applied Power Electronics Conference and Exposition (APEC)*, 2016, pp. 1534–1540.
- [8] J. Sun, W. Chen, and X. Yang, "EMI prediction and filter design for MHz GaN based LLC half-bridge converter," in *2016 IEEE 8th International Power Electronics and Motion Control Conference (IPEMC-ECCE Asia)*, 2016, pp. 297–304.
- [9] Q. Yu and T. Holmes, "A study on stray capacitance modeling of inductors by using the finite element method," *IEEE Transactions on Electromagnetic Compatibility*, vol. 43, no. 1, pp. 88–93, 2001.
- [10] M. Kovačić, S. Stipetić, Z. Hanić, and D. Žarko, "Small-signal calculation of common-mode choke characteristics using finite-element method," *IEEE Transactions on Electromagnetic Compatibility*, vol. 57, no. 1, pp. 93–101, 2015.
- [11] C. Cuellar and N. Idir, "Stray capacitances determination methods of EMI filter inductors," in *IECON 2017 - 43rd Annual Conference of the IEEE Industrial Electronics Society*, 2017, pp. 7040–7045.
- [12] M. Bensteti, Y. Le Bihan, C. Marchand, C.-M. Tasseti, G. Lissorgues, E. Gergam, and J.-P. Gilles, "A hybrid finite-element method for the modeling of microcoils," *IEEE Transactions on Magnetics*, vol. 41, no. 5, pp. 1868–1871, 2005.
- [13] A. Chafi, N. Idir, A. Videt, and H. Maher, "Design method of PCB inductors for high-frequency power converters," *IEEE Transactions on Power Electronics*, vol. 36, no. 1, pp. 805–814, 2021.
- [14] L. Dalessandro, F. da Silveira Cavalcante, and J. W. Kolar, "Self-capacitance of high-voltage transformers," *IEEE Transactions on Power Electronics*, vol. 22, no. 5, pp. 2081–2092, 2007.
- [15] Z. Shen, H. Wang, Y. Shen, Z. Qin, and F. Blaabjerg, "An improved stray capacitance model for inductors," *IEEE Transactions on Power Electronics*, vol. 34, no. 11, pp. 11 153–11 170, 2019.
- [16] H. Zhao, D. N. Dalal, A. Bjørn Jørgensen, J. K. Jørgensen, X. Wang, S. Bęczkowski, S. Munk-Nielsen, and C. Uhrenfeldt, "Physics-based modeling of parasitic capacitance in medium-voltage filter inductors," *IEEE Transactions on Power Electronics*, vol. 36, no. 1, pp. 829–843, 2021.
- [17] B. Liu, R. Ren, F. Wang, D. Costinett, and Z. Zhang, "Winding scheme with fractional layer for differential-mode toroidal inductor," *IEEE Transactions on Industrial Electronics*, vol. 67, no. 2, pp. 1592–1604, 2020.
- [18] Y. Li and S. Wang, "Modeling and increasing the high-frequency impedance of single-layer Mn-Zn ferrite toroidal inductors with electro-magnetic analysis," *IEEE Transactions on Power Electronics*, vol. 36, no. 6, pp. 6943–6953, 2021.
- [19] A. Massarini and M. Kazimierczuk, "Self-capacitance of inductors," *IEEE Transactions on Power Electronics*, vol. 12, no. 4, pp. 671–676, 1997.
- [20] M. Kovacic, Z. Hanic, S. Stipetic, S. Krishnamurthy, and D. Zarko, "Analytical wideband model of a common-mode choke," *IEEE Transactions on Power Electronics*, vol. 27, no. 7, pp. 3173–3185, 2012.
- [21] N. B. Chagas and T. B. Marchesan, "Analytical calculation of static capacitance for high-frequency inductors and transformers," *IEEE Transactions on Power Electronics*, vol. 34, no. 2, pp. 1672–1682, 2019.
- [22] G. Dong, F. Zhang, Y. Liu, W. Meng, and C. Xu, "Analytical method for extraction of stray capacitance in single-layer CM chokes," in *2019 IEEE Energy Conversion Congress and Exposition (ECCE)*, 2019, pp. 3185–3191.
- [23] L. Middelstädt, S. Skibin, R. Döbelin, and A. Lindemann, "Analytical determination of the first resonant frequency of differential mode chokes by detailed analysis of parasitic capacitances," in *2014 16th European Conference on Power Electronics and Applications*, 2014, pp. 1–10.
- [24] A. Massarini, "Analytical approach to the calculation of parasitic capacitance between winding turns," in *2018 IEEE 4th International Forum on Research and Technology for Society and Industry (RTSI)*, 2018, pp. 1–4.
- [25] F. Salomez, A. Videt, and N. Idir, "Semi-analytical model of parasitic capacitance of inductor with conductive core," in *PCIM Europe digital days 2021: International Exhibition and Conference for Power Electronics, Intelligent Motion, Renewable Energy and Energy Management*, 2021, pp. 1–8.
- [26] F. Salomez, A. Videt, and N. Idir, "Modelling and minimization of the parasitic capacitance of ring core inductors," in *2021 23rd European Conference on Power Electronics and Applications (EPE'21 ECCE Europe)*, 2021, pp. 1–10.
- [27] S. W. Pasko, M. K. Kazimierczuk, and B. Grzesik, "Self-capacitance of coupled toroidal inductors for EMI filters," *IEEE Transactions on Electromagnetic Compatibility*, vol. 57, no. 2, pp. 216–223, 2015.
- [28] W. Tan, X. Margueron, and N. Idir, "Analytical modeling of parasitic capacitances for a planar common mode inductor in EMI filters," in *2012 15th International Power Electronics and Motion Control Conference (EPE/PEMC)*, 2012, pp. DS3f.2–1–DS3f.2–6.
- [29] E. Snelling, *Soft ferrites: properties and applications*. Iliffe Books Ltd, 1969, ch. 11.
- [30] M. Zdanowski, K. Kostov, J. Rabkowski, R. Barlik, and H.-P. Nee, "Design and evaluation of reduced self-capacitance inductor in DC/DC converters with fast-switching SiC transistors," *IEEE Transactions on Power Electronics*, vol. 29, no. 5, pp. 2492–2499, 2014.
- [31] R. Clarke. (2007, March) The wave winder. [Online]. Available: <http://info.ee.surrey.ac.uk/Workshop/advice/coils/winders/wave/index.html>
- [32] H. Zhao, S. Luan, Z. Shen, A. J. Hanson, Y. Gao, D. N. Dalal, R. Wang, S. Zhou, and S. Munk-Nielsen, "Rethinking basic assumptions for modeling parasitic capacitance in inductors," *IEEE Transactions on Power Electronics*, vol. 37, no. 7, pp. 8281–8289, 2022.
- [33] D. C. Meeker, "Finite Element Method Magnetics, ver. 4.2, (21 April 2019 build)," Software. [Online]. Available: <https://www.femm.info>
- [34] S. Diaham and M.-L. Locatelli, "Dielectric properties of polyamide-imide," *Journal of Physics D: Applied Physics*, vol. 46, no. 18, p. 185302, apr 2013.
- [35] J. Zechmeister and J. Lacik, "Complex relative permittivity measurement of selected 3D-printed materials up to 10 GHz," in *2019 Conference on Microwave Techniques (COMITE)*, 2019, pp. 1–4.
- [36] P.-E. Lévy, F. Costa, C. Gautier, and B. Revol, "Analytical calculation of the magnetic field radiated by a CM coil using conformal mapping methods," in *2014 International Symposium on Electromagnetic Compatibility*, 2014, pp. 246–251.



**Florentin Salomez** Florentin Salomez received the master's degree in Electrical Engineering from the University of Lille, Lille, France, in 2018 and the master's degree in Engineering from the Hautes Etudes d'Ingénieur, Lille, France, in 2018.

He is working toward the Ph.D degree in electrical engineering at the L2EP Laboratory, University of Lille, Lille, France.

His research interests include passive EMI filter designs, magnetic materials used in power electronics, and electromagnetic simulations.



**Arnaud Videt** Arnaud Videt (Member, IEEE) received the Ph.D. degree in electrical engineering from Ecole Centrale de Lille, Villeneuve-d'Ascq, France, in 2008. He joined Schneider Toshiba Inverter, Pacy-sur-Eure, France, where his research focused on motor drive converter topologies, power quality, and modulation strategies. Since 2010, he is an Associate Professor with the L2EP Laboratory, University of Lille, Lille, France. His research interests include wide-bandgap power devices, HF converter design, and electromagnetic compatibility

issues in power converters.



**Nadir Idir** Nadir Idir (M'93) received the Ph.D. degree in electrical engineering from the University of Lille, Lille, France, in 1993. He is currently a Full Professor with IUT, University of Lille, Villeneuve-d'Ascq, France, where he teaches power electronics and electromagnetic compatibility. Since 1993, he has been with the Laboratory of Electrical Engineering and Power Electronics (L2EP), University of Lille. Since 2022, he has been the Head of the Power Electronics team of L2EP. His research interests include design methodologies for HF switching

converters, characterization and modeling of wide bandgap semiconductors, integration in power electronics, electromagnetic interference (EMI) in static converters, HF modeling of the magnetic components, and EMI filter design methodologies for power converters.